

Northumbria Research Link

Citation: Cao, Keshuang, Zhao, Xitong, Chen, Jian, Xu, Bin, Shahzad, Muhammad Wakil, Sun, Wenping, Pan, Hongge, Yan, Mi and Jiang, Yinzhu (2022) Hybrid design of bulk-Na metal anode to minimize cycle-induced interface deterioration of solid Na metal battery. *Advanced Energy Materials*, 12 (7). p. 2102579. ISSN 1614-6832

Published by: Wiley-Blackwell

URL: <https://doi.org/10.1002/aenm.202102579>
<<https://doi.org/10.1002/aenm.202102579>>

This version was downloaded from Northumbria Research Link:
<https://nrl.northumbria.ac.uk/id/eprint/48008/>

Northumbria University has developed Northumbria Research Link (NRL) to enable users to access the University's research output. Copyright © and moral rights for items on NRL are retained by the individual author(s) and/or other copyright owners. Single copies of full items can be reproduced, displayed or performed, and given to third parties in any format or medium for personal research or study, educational, or not-for-profit purposes without prior permission or charge, provided the authors, title and full bibliographic details are given, as well as a hyperlink and/or URL to the original metadata page. The content must not be changed in any way. Full items must not be sold commercially in any format or medium without formal permission of the copyright holder. The full policy is available online: <http://nrl.northumbria.ac.uk/policies.html>

This document may differ from the final, published version of the research and has been made available online in accordance with publisher policies. To read and/or cite from the published version of the research, please visit the publisher's website (a subscription may be required.)

Hybrid design of bulk-Na metal anode to minimize cycle-induced interface deterioration of solid Na metal battery

*Keshuang Cao, Xitong Zhao, Jian Chen, Ben Bin Xu, Muhammad Wakil Shahzad, Wenping Sun, Hongge Pan, Mi Yan, Yinzhu Jiang**

K. Cao, X. Zhao, Prof. W. Sun, Prof. H. Pan, Prof. M. Yan, Prof. Y. Jiang
School of Materials Science and Engineering, State Key Laboratory of Clean Energy Utilization, Zhejiang University, Hangzhou 310027, P. R. China
E-mail: yzjiang@zju.edu.cn

K. Cao, Prof. Y. Jiang
ZJU-Hangzhou Global Scientific and Technological Innovation Centre, Zhejiang University, Hangzhou 311200, P.R. China

Prof. J. Chen, Prof. H. Pan
Institute of Science and Technology for New Energy, Xi'an Technological University, Xi'an 710021, P.R. China

Prof. B. B. Xu, Dr. M.W. Shahzad
Mechanical and Construction Engineering, Faculty of Engineering and Environment, Northumbria University, Newcastle upon Tyne NE1 8ST, UK

Keywords: Na metal anode, solid-state batteries, NaSICON, interface resistance, cycling stability

The pursuit for high-energy and intrinsically safe energy storage has been significantly driving the development of solid-state alkali metal batteries. The interfacial contact between metal anode and solid electrolyte plays a key role enabling stable cycling of solid batteries. However, the sluggish alkali atom replenishment rate during stripping will unavoidably lead to the interface deterioration that destroys the initial physical contact by forming the interfacial voids and triggers the dendrite growth. Herein, we propose a hybrid bulk Na anode approach by incorporating ion-conducting phase into

metallic Na matrix, constructing abundant interfacial electrochemical reaction area and enabling a balanced Na replenishment and consumption to minimize cycle-induced interface deterioration. Specific attention is paid to the effects of the second phase on the wettability and creep ability of hybrid Na metal. A high critical current density (3.1 mA cm^{-2}) and long cycling life (6000 h in 0.5 mA cm^{-2}) are achieved for the symmetric cells. Full cells coupling the hybrid anode with the $\text{Na}_3\text{V}_2(\text{PO}_4)_3/\text{C}$ cathode delivers excellent cyclability over 7300 cycles at a high rate of 5 C. The viewpoint from balancing consumption and replenishment rate of metal atoms pave a new way for designing cycle-stable anode/electrolyte interface in solid-state batteries.

1. Introduction

There is an ever-increasing demand for high-energy and intrinsically-safe energy storage techniques, in response to the global action of ‘Net Zero’ and the concerns on the recurring safety issues from lithium ion batteries (LIBs).^[1] Solid-state batteries (SSBs) based on solid electrolytes (SEs) have been considered as the most promising candidate for next-generation rechargeable battery.^[2] Among those solid-state lithium batteries investigated by far, solid sodium batteries coupled with Na metal anode and Na-ion conducting SEs show further competitiveness due to the rich resource of Na.^[1a, 3] However, unlike the unobstructed solid-liquid interface in LIBs, the poor contact of solid-solid interface in SSBs amplifies the interface resistance, which has become one of main culprits in the practical applications of SSBs.^[4]

Considerable efforts have been devoted to improve the interfacial contact by adjusting the wettability between Li/Na metal anode and SEs, by modifying the surface

of SEs with Al_2O_3 ,^[5] TiO_2 ,^[6] AlF_3 ,^[7] and SnO_2 .^[8] Further practices to optimize the wettability also include the hybrid bulk design for alkali metal anode, such as introducing graphite,^[9] boronnitride (BN)^[10], SiO_2 ^[11] or Si_3N_4 ^[12] in Li/Na metal. It is worth mentioning that the hybrid bulk design can do more than that, it endows more feasibility for alkali metal anode by altering its original characteristics.^[13] Although the initial contact between Li/Na metal and SEs has been well remediated through the above strategies, the interfacial contact will inevitably deteriorate along with the Li/Na plating/stripping processes, especially at high current density. P.G. Bruce *et. al*^[14] observed the severe void formation and accumulation on cycling due to the untimely Li replenishment during the Li stripping process, resulting into the dendrite formation on plating, subsequently causing short circuit and cell failure. A recent study^[15] identified the void as the primary reason caused cell failure, after visualizing the void formation under operando synchrotron X-ray tomography. From this perspective, the impact of cycle-induced interface deterioration in SSBs appears to be substantial, which has been underestimated for a long time.

Herein, a hybrid bulk Na metal anode is developed by incorporating solid electrolyte particles with high ionic conductivity and chemical stability in molten Na metal to minimize cycle-induced interfacial deterioration of solid sodium battery (**Figure 1**). In this concept, the wettability of sodium and inorganic SE can be significantly improved to achieve the intimate contact of the initial interface. More importantly, the local sodium consumption rate can be regulated by the ion/electron-transfer interfaces constructed in the hybrid anode, which makes the consumption and the replenishment

rate match to minimize the cycle-induced interface evolution. Benefiting from above, the hybrid Na anodes deliver stable cycling for 6000 h at 0.5 mA cm^{-2} in symmetric cells and enable NVP/NZSP/hybrid Na full cells with at least 7300 stable cycles in high current rate of 5 C.

2. Results and discussion

A NaSICON-type Na^+ superionic conductor $\text{Na}_{3.4}\text{Zr}_2\text{Si}_{2.4}\text{P}_{0.6}\text{O}_{12}$ (NZSP, the ionic conductivity value = 4.1 mS cm^{-1} , Figure S1) was used as solid electrolyte for the construction of SSBs. The hybrid design of bulk Na-metal-based anode was realized through a facile melt infusion method, by immersing the NZSP powders into the molten Na metal. A conformal SnO_2 layer was pre-coated on the surface of NZSP powders to improve their affinity to Na metal (Figure S2 and S3), through the spontaneous alloying reaction between molten Na and SnO_2 . After $\text{SnO}_2@\text{NZSP}$ was mixed with molten Na, NZSP phase transformation was not detected in the XRD results (Figure 2a) and X-ray photoelectron spectroscopy (XPS) analysis (Figure S4). Although the SEI layer will be formed when NZSP contacts with highly reactive Na metal, it is relatively thin (only a few nm thick) and kinetically stable.^[16] As expected, the physical contact between NZSP solid electrolyte and Na metal, even the molten state of Na, seems quite poor (Figure 2b). Molten Na appears as a bead on NZSP pellet with a high contact angle of 135 degrees, which can roll freely on the NZSP pellet (Figure S5). When the Na foil is attached to the NZSP pellet under external force, gaps remain in the interface between Na and NZSP (Figure 2f) despite the good ductility of Na metal. On the contrast, hybrid anodes with different NZSP content exhibit much improved wettability with NZSP

pellet (Figure 2e and S6). A contact angle of 83 degrees for the hybrid anode in the composition of NZSP:Na = 1:5 (mass ratio, Figure 2c). Moreover, a droplet of hybrid anode can be pinned on the NZSP pellet without rolling off when the pellet is tilted (Figure 2d). The enhanced physical contact between hybrid anode and NZSP pellet is further evidenced by the cross-sectional SEM image (Figure 2g), where an intimate contact is observed on the hybrid Na/NZSP interface.

Apart from the direct observation, the interfacial charge transfer resistance is an important indicator to justify the practical solid-solid contact on the interface. To optimize the bulk anode design, a series of hybrid anodes are constructed with variation in composition of Na and NZSP, which were tested through electrochemical impedance spectroscopy (EIS, Figure S7). In **Figure 3a**, it is shown that the interfacial resistance of the hybrid anode gradually decrease with the increase of NZSP content, and reach a valley value of $2.4 \Omega \text{ cm}^2$ (only one fifth of that of the pristine Na anode) for the composition of NZSP:Na = 1:1 (mass ratio, the following descriptions of composition are all mass ratios). Besides the improved wettability for the hybrid anode, the reduced interface resistance can also be ascribed to the enlarged electron/ion boundaries for fast charge transfer process.^[17]

It is worth noting that the interfacial contact between the anode and solid electrolyte might undergo enormous deterioration during Na plating/stripping process, particularly cycling under the high current density, large areal capacity and long-term period.^[18] Recent studies^[19] have shown that voids will be formed on the interface during Li/Na stripping, if the rate of replenishing Li/Na atoms from both creep and atomic diffusion

in the metal anode cannot reach the stripping current for Li/Na removing from the interface. This is also the reason why external force is preferred to operate SSBs, to promote the metal creep ability and minimize the formation of stripping-induced voids. Whilst we can reduce the initial interface resistance by adding more NZSP content in the hybrid anode to enlarge and elongate interfaces for charge transfer, this will unavoidably increase the anode hardness (Figure 3a) and correspondingly slow down the rate of Na metal creep.

Therefore, a balanced Na-metal creep and ion/electron reaction interface is highly desired to minimize the cycling-induced interface evolution and improve the cell cycling performance. Critical current density (CCD), defined as the largest current density that the solid electrolyte can endure the dendrite penetration, is a critical parameter to assess the interfacial stability between anode and solid electrolyte. As shown in Figure 3c, the overpotential of the Na symmetric cell is unstable during cycling, indicating the degradation of the Na/SE interface, followed by the sudden occurrence of short circuit at 0.5 mA cm^{-2} . In contrast, the CCD of all hybrid Na cells are higher than that of pristine Na cell (Figure 3d and S8), indicating that the interfacial stability of the Na/SE interface is enhanced by such hybrid Na design with adding NZSP.

Interestingly, the NZSP:Na = 1:5 cell with moderate interface resistance ($3.5 \text{ } \Omega \text{ cm}^2$) and hardness (91 HC) presents the low and stable overpotential with the largest CCD of 3.1 mA cm^{-2} , than that of the cell with hybrid electrode of NZSP:Na = 1:1 which has the minimum interface resistance. When mixing the ion-insulating zirconia powder

(ZrO₂, with the particle size similar to the NZSP used in this research, Figure S9) with Na metal in the same way (ZrO₂-Na hybrid anode, the same volume fraction as NZSP:Na = 1:5), we can also achieve the improvement on the wettability of Na and NZSP (Figure S10). But its interface resistance remains larger than that of NZSP-Na anode, and its CCD is also significantly smaller than that of NZSP-Na anode (Figure S11). The SnO₂-Na hybrid anode prepared show similar test results as that of ZrO₂-Na (Figure S12), indicating that the high ionic conductivity of NZSP is essential to improve the battery's tolerance for higher current density, which may create more ion-electron electrochemical reaction interface.^[13b]

From above, the mixing ratio of NZSP and Na to reach the optimized state for hybrid anode takes as 1:5, denoted as h-Na. In the long-term cycling tests (**Figure 4a**), the overpotential of the Na symmetric cell increases rapidly in the first few cycles (increase from the initial 8 mV to 0.1 V only in the 4th cycle). Then, the overpotential appears to be unstable with a short circuit occurs at 82 h. After performing a postmortem examination on the failed cell (Figure S13), some black ablation areas can be observed on the surface of NZSP pellet, which is probably to be the Na penetration caused by the interfacial contact loss.^[20] In comparison, the symmetric cell with h-Na anode shows the long-term stability with a small polarization (5 mV) over 6000 h (Figure S14) under the same test conditions. Even at a higher current density of 0.5 mA cm⁻² (Figure 4b), the h-Na symmetric cell remains stable, and polarization stays below 25 mV in the 6000 h (12000 cycles, and the battery is cycling stably so far). Furthermore, the interface resistance of Na symmetric cell increases greatly after 10 cycles from 12.0 to 345.3 Ω

cm^2 (Figure 4c). Nevertheless, the interface resistance of the h-Na symmetric cell only increases from 3.5 to 4.7 $\Omega \text{ cm}^2$ in the first 100 cycles (Figure 4d), indicating a ultrastable interface between h-Na and SE. SEM observation also suggests that the h-Na/SE interface remains intimate contact after 100 cycles (Figure S15).

We next evaluate the temporal evolution of the interface during cycling, by using operando galvanostatic electrochemical impedance spectroscopy (GEIS, **Figure 5a, b**). The pristine Na and h-Na anodes are anodized at an apparent (geometrical) current density of 200 $\mu\text{A cm}^{-2}$. According to the previous reports,^[19] the increase of polarization is mainly caused by the stripping of Na under galvanostatic polarization, and the influence of plating can be ignored in symmetric cell. With the stripping of Na, the overpotential of pristine Na symmetric cell increases rapidly, to reach 0.2 V at 200 min (Figure 5c) with a consistent change in interface resistance (Figure 5a). On the contrary, the overpotential of the h-Na symmetric cell remains stable at below 20 mV for the first 300 min, and then suddenly increases at 350 min to reach 0.2 V at 370 min (Figure 5d). The above results suggest that the stripping of Na easily leads to the deterioration of the pristine Na/SE interface, and the interface between h-Na and SE can accommodate a deeper discharge depth. The SEM observation discover several small voids with a width of about 20 μm on the interface of pristine Na/SE, after stripping for 150 min. The observed voids seem quite different from the interfacial voids caused by mechanical bonding, which usually have larger size (over 100 μm , Figure 2f). On the contrary, no voids can be observed on the interface of h-Na/SE.

To further understand the electrochemical process at the interface, the kinetics of

anode/SE interface was exploited by EIS and Tafel plots. The apparent diffusion coefficient of Na^+ (D_{Na^+}) is numerically estimated by fitting the low-frequency region of the Nyquist plots of full cells assembled with NVP cathodes (**Figure 6a** and S16). The two orders of magnitude higher value of D_{Na^+} in the h-Na cell (5.3×10^{-14} vs. $6.6 \times 10^{-15} \text{ cm}^2 \text{ s}^{-1}$ of bare Na, Figure 6b) indicates that the NZSP skeleton with fast ionic conductivity effectively enhances the electrochemical kinetics in h-Na. The exchange current density of the cell can be obtained by fitting the high overpotential region in Tafel plots (Figure 6c). The h-Na symmetric cell exhibits a significantly increased exchange current density of 1.08 mA cm^{-2} in comparison to 0.47 mA cm^{-2} for the pristine Na symmetric cell (Figure 6d), suggesting a faster ionic transfer kinetics for the h-Na/SE interface.^[21]

During stripping, the stripped Na metal atoms will generate equivalent vacancies, which will accumulate into voids if supersaturation due to high stripping current occurs.^[19b] The consumed flux of Na atom (J_{consume}) is proportional to the applied current (i) and inversely proportional to the effective reaction area (A_{eff}), as it can be expressed by Equation (1).^[14, 22] On the other hand, the creep and diffusion of the sodium metal will prompt the sodium atoms replenish the vacancy, where the replenished sodium atom flux can be expressed in Equation (2).^[22]

$$J_{\text{consume}} = \frac{i}{A_{\text{eff}} \cdot e} \quad (1)$$

$$J_{\text{replenish}} = J_{\text{creep}} + J_{\text{diffusion}} \quad (2)$$

The creep and diffusion rate mainly relate to the intrinsic properties of the sodium metal and the external pressure and temperature. When $J_{\text{consume}} > J_{\text{replenish}}$, the consumption

rate of sodium atoms is faster than it can be replenished, vacancies accumulate at the interface to form voids and lead to the deterioration of the interface. When $J_{\text{consume}} \leq J_{\text{replenish}}$, the rate of sodium atoms replenishing vacancies is fast enough that the interface remains stable without voids during sodium stripping, which is desired. As shown in the previous test results, the introduction of NZSP particles in the h-Na brings high ionic conductivity component to enable the electrochemical reaction not limited to the contact plane between SE pellet and the Na metal foil. The ions can continue to transmit along the NZSP skeleton to the inner of the h-Na, resulting in more ion-electron interfaces for reaction, thus, A_{eff} is increased. As it can be seen from Equation (1), J_{consume} decreases with the increase of A_{eff} at the same current, which means the consumption rate of local metal atoms decreases. However, the introduction of NZSP increases the hardness of h-Na and then slows down the creep rate, thus reducing the $J_{\text{replenish}}$. The higher content of NZSP can increase A_{eff} and reduce the vacancy formation rate, but excessive NZSP reduces the creep rate and the vacancy replenishing rate of sodium atoms. Therefore, the discovery of the optimal content of NZSP (Figure 3a, b) that can balance the J_{consume} and $J_{\text{replenish}}$ is meaningful for the future applications.

Full battery cells with $\text{Na}_3\text{V}_2(\text{PO}_4)_3/\text{C}$ (NVP) cathode and NZSP electrolyte were constructed using Na anode and h-Na anode respectively, to further evaluate the performance of h-Na anode. The characterization results of NVP cathode are presented in supplementary information (Figure S17). A small amount of carbonate-based electrolyte was adopted to wet the cathodic side. NZSP is confirmed to be electrochemically stable to Na metal in the tested voltage range by cyclic voltammetry

(CV) and linear sweep voltammetry (LSV) (Figure S18). As shown in **Figure 7a**, the Coulombic efficiency (CE) of NVP/NZSP/Na cell fluctuates significantly after 500 cycles, followed by rapid capacity fading and battery failure. The voltage curve shows that the battery cannot charge normally during the CE fluctuation, which is probably caused by soft short circuit (Figure S19). Impressively, the h-Na cell delivers a high initial discharge capacity of 110.7 mAh g⁻¹, retaining a superior reversible capacity of 93.9 mAh g⁻¹ after 7300 cycles with an average CE of 99.8%. The polarization remains almost constant over 1000 cycles (Figure 7b), suggesting the excellent cycle stability of the cell. Moreover, we demonstrate a longer life span and a higher capacity retention rate than other studies reported on solid-state sodium metal batteries based on NVP cathodes (Figure 7c), because of the stabilized anode/SE interface.

3. Conclusion

In summary, a hybrid Na anode strategy with incorporating high ionic conductivity NZSP particles is described, to simultaneously solve the problems of poor initial interface contact and cycle-induced interface deterioration on the anode/SE interface. The introduction of NZSP particles enables an intimate contact between Na and SE by increasing the viscosity of Na metal, thus significantly reduces the initial interface resistance. The uniformly distributed NZSP particles with high ionic conductivity also extend the electrochemical reaction area. The theoretical understanding unveils a reduction on the local vacancy formation for the abundant reaction zone, enabling the vacancy formation and replenishment rate match and stabilizing the interface without the formation of voids. As a result, the interface resistance with hybrid Na is reduced

to $2.4 \Omega \text{ cm}^2$, and the CCD is increased significantly to 3.1 mA cm^{-2} . Meanwhile, galvanostatic cycling of symmetric cells remained stable over 4000 h with low overpotential at 0.5 mA cm^{-2} , and the full cells with hybrid Na exhibited excellent cycling and rate performance. This work provides new insights to design novel alkali metal-based anodes by minimizing the cycle-induced interface deterioration toward long-term stable cycling in solid-state batteries.

4. Experimental Section

Materials synthesis: Primary $\text{Na}_{3.4}\text{Zr}_2\text{Si}_{2.4}\text{P}_{0.6}\text{O}_{12}$ (NZSP) powder was synthesized through a solution-assisted solid-state reaction method as previously reported.^[23] To obtain solid electrolyte pellets, 500 mg primary powder was put into a cylindrical stainless-steel mold with a diameter of 12.7 mm and pressed at 400 Mpa. Then, the pressed pellets were sintered at 1310°C for 6 h in air. The sintered pellet is about 11 mm in diameter and 1.6 mm in thickness.

Some primary powder was calcined at 1100°C for 3 h to improve the crystallinity of NZSP. Then, the NZSP powder was coated with SnO_2 to enhance its affinity with sodium metal with an impregnation-sintering process as our previous report.^[24] Specifically, the NZSP powder was mixed in an N, N-dimethylformamide (DMF) solution of $0.5 \text{ mol L}^{-1} \text{ SnCl}_2$, and the mass of SnCl_2 in the solution was 15 wt% of NZSP powder. After stirring for 2 hours, the solution was dried and calcined in air at 450°C for 2 hours to obtain $\text{SnO}_2@\text{NZSP}$ powder. Next, NZSP and Na metal were weighed and put into a nickel crucible in an argon-filled glove box ($\text{O}_2 \leq 0.1 \text{ ppm}$, $\text{H}_2\text{O} \leq 0.1 \text{ ppm}$), then stirred at 250°C for 5 minutes, to form a metallic liquid slurry, which

has great wettability with NZSP pellets. Finally, it was uniformly spread over the NZSP pellets by a scraper to apply as the anode.

$\text{Na}_3\text{V}_2(\text{PO}_4)_3/\text{C}$ was prepared by the same process as previously reported.^[25] Typically, $\text{NH}_4\text{H}_2\text{PO}_4$ and NaOH were added into NH_4VO_3 aqueous solution according to stoichiometric ratio at 80 °C with stirring. Then, citric acid with the same molar amount as vanadium source was added as carbon source and reducing agent. After stirring, the solution was dried overnight, and the residual product was sintered at 800 °C for 10 h in Ar atmosphere to obtain $\text{Na}_3\text{V}_2(\text{PO}_4)_3/\text{C}$.

Materials characterization: X-ray diffraction (XRD) characterization was performed on an X-ray diffractometer (Bruker D8 Advance, Germany) with Co K_α radiation ($k = 1.7902 \text{ \AA}$) at 35 kV, 28 mA. SEM observations were carried on a field-emission scanning electron microscopy (SU-8010, Hitachi). Elemental mapping was obtained from an energy dispersive X-ray spectroscope (X-max 80, Oxford). A Shore C durometer (LX-C) was employed to analyze the hardness of pristine Na and hybrid Na.

Electrochemical measurements: The ionic conductivity of sintered NZSP pellets was calculated from electrochemical impedance spectroscopy (EIS) with data collected by a CHI660C electrochemical workstation in the frequency range from 1 MHz to 1 Hz with a 5 mV amplitude, in which gold was sputtered on both sides as blocking electrodes. The EIS data of symmetric cells were obtained under the same frequency range. In order to get more information in the low frequency region, impedance spectra of full cells were recorded in the frequency range from 1 MHz to 0.1 Hz with a 5 mV amplitude.

The standard CR2032 coin-type cells were assembled in an Ar-filled glove box to be used to evaluate the electrochemical performance of different electrodes. For the assemble of hybrid Na symmetric cells, 0.006 g of the NZSP/Na mixture was evenly spread over both sides of NZSP pellets as electrodes. For the pristine Na symmetric cells, a fresh Na metal block was punched into discs with a diameter of 1.1 cm, then it was immediately pressed on both sides of NZSP pellets by hand. All coin cells were encapsulated with a packaging machine (MSK-160E) under 0.6 tons of force and tested after standing for 2 hours. For the operando galvanostatic electrochemical impedance spectroscopy (GEIS) measurements, the symmetric cells were galvanostatic polarized at 0.2 mA cm^{-2} . The GEIS was captured every 10 minutes at a current density of 0.2 mA cm^{-2} with a sinusoidal current of $10 \text{ } \mu\text{A cm}^{-2}$ in the frequency range from 1 MHz to 1 Hz by using an IviumNstat equipment (Ivium, Netherlands).

For the full cells with NVP cathode, $\text{Na}_3\text{V}_2(\text{PO}_4)_3/\text{C}$ was ground with NZSP powder and Super P at a mass ratio of 60 : 38 : 2 and sintered at $750 \text{ }^\circ\text{C}$ for 5 h in Ar containing 5% H_2 . The cathode slurry was prepared by mixing the mixture, poly(vinylidene fluoride) (PVDF) and Super P in a weight ratio of 8:1:1 in N-methyl-2-pyrrolidone (NMP) solvent. The slurry was dried at $80 \text{ }^\circ\text{C}$ in vacuum overnight after casting on the NZSP pellets. Excluding the inactive materials, the mass loading of active materials NVP was about 1 mg cm^{-2} . Then, Au was sputtered on the surface of the cathode as current collector. NZSP pellets with cathode were then transferred to an Ar-filled glove box to assemble the full cells. The anode was prepared by the same method mentioned above, and a small amount of liquid electrolyte (1 M NaPF_6 in EC/DEC/PC (4:4:2,

volume ratio) with the addition of 5% FEC) was added to wet NVP and the interface between NZSP and NVP cathode. Galvanostatic cycling experiments for all batteries were performed on the Neware battery test system (Neware BTS-5).

Supporting Information

Supporting Information is available from the Wiley Online Library or from the author.

Acknowledgements

This work was supported by the National Key Research and Development Program (2019YFE0111200), Zhejiang Provincial Natural Science Foundation of China (LR18B030001) and the Fundamental Research Funds for the Central Universities.

Received: ((will be filled in by the editorial staff))

Revised: ((will be filled in by the editorial staff))

Published online: ((will be filled in by the editorial staff))

References

- [1] a) J. A. S. Oh, L. He, B. Chua, K. Zeng, L. Lu, *Energy Storage Mater.* **2021**, 34, 28; b) Y. Lu, C. Zhao, H. Yuan, X. Cheng, J. Huang, Q. Zhang, *Adv. Funct. Mater.* **2021**, 31, 2009925; c) H. Xia, Y. Tang, O. I. Malyi, Z. Zhu, Y. Zhang, W. Zhang, X. Ge, Y. Zeng, X. Chen, *Adv. Mater.* **2021**, 33, 2004998
- [2] a) J. Wu, L. Yuan, W. Zhang, Z. Li, X. Xie, Y. Huang, *Energy Environ. Sci.* **2021**, 14, 12; b) B. Tang, P. W. Jaschin, X. Li, S.-H. Bo, Z. Zhou, *Mater. Today* **2020**, 41, 200-218.
- [3] a) H. Yang, B. Zhang, K. Konstantinov, Y. Wang, H. Liu, S. Dou, *Advanced Energy and Sustainability Research* **2021**, 2, 2000057; b) S. Ferrari, M. Falco, A. B. Muñoz-García, M. Bonomo, S. Brutti, M. Pavone, C. Gerbaldi, *Adv. Energy Mater.*

- 2021**, 2100785. c) M. Chen, Q. Liu, Z. Hu, Y. Zhang, G. Xing, Y. Tang, S. Chou, *Adv. Energy Mater.* **2020**, 10, 2002244.
- [4] Z. Li, P. Liu, K. Zhu, Z. Zhang, Y. Si, Y. Wang, L. Jiao, *Energy & Fuels* **2021**, 35, 9063.
- [5] X. Han, Y. Gong, K. Fu, X. He, G. T. Hitz, J. Dai, A. Pearse, B. Liu, H. Wang, G. Rubloff, Y. Mo, V. Thangadurai, E. D. Wachsman, L. Hu, *Nat. Mater.* **2016**, 16, 572.
- [6] J. Yang, Z. Gao, T. Ferber, H. Zhang, C. Guhl, L. Yang, Y. Li, Z. Deng, P. Liu, C. Cheng, R. Che, W. Jaegermann, René Hausbrand, Y. Huang, *J. Mater. Chem. A* **2020**, 8, 7828.
- [7] X. Miao, H. Di, X. Ge, D. Zhao, P. Wang, R. Wang, C. Wang, L. Yin, *Energy Storage Mater.* **2020**, 30, 170.
- [8] B. Tang, L. Gao, J. Liu, S. Bo, Z. Xie, J. Wei, Z. Zhou, *J. Mater. Chem. A* **2020**, 8, 18087.
- [9] J. Duan, W. Wu, A. M. Nolan, T. Wang, J. Wen, C. Hu, Y. Mo, W. Luo, Y. Huang, *Adv. Mater.* **2019**, 31, 1807243.
- [10] J. Wen, Y. Huang, J. Duan, Y. Wu, W. Luo, L. Zhou, C. Hu, L. Huang, X. Zheng, W. Yang, Z. Wen, Y. Huang, *ACS Nano* **2019**, 13, 14549.
- [11] H. Fu, Q. Yin, Y. Huang, H. Sun, Y. Chen, R. Zhang, Q. Yu, L. Gu, J. Duan, W. Luo, *ACS Mater. Lett.* **2020**, 2, 127.
- [12] M. Du, Y. Sun, B. Liu, B. Chen, K. Liao, R. Ran, R. Cai, W. Zhou, Z. Shao, *Adv. Funct. Mater.* **2021**, 2101556

- [13] a) Y. Huang, B. Chen, J. Duan, F. Yang, T. Wang, Z. Wang, W. Yang, C. Hu, W. Luo, Y. Huang, *Angew. Chem. Int. Ed.* **2020**, 59, 3699; b) Q. Liu, G. Zhu, R. Li, S. Lou, H. Huo, Y. Ma, J. An, C. Cao, F. Kong, Z. Jiang, M. Lu, Y. Tong, L. Ci, G. Yin, J. Wang, *Energy Storage Mater.* **2021**, 41, 1-7; c) D. Lin, J. Zhao, J. Sun, H. Yao, Y. Liu, K. Yan, Y. Cui, *Proc. Natl. Acad. Sci. U. S. A.* **2017**, 114, 4613; d) L. Fan, S. Li, L. Liu, W. Zhang, L. Gao, Y. Fu, F. Chen, J. Li, H. L. Zhuang, Y. Lu, *Adv. Energy Mater.* **2018**, 8, 1802350.
- [14] J. Kasemchainan, S. Zekoll, D. Spencer Jolly, Z. Ning, G. O. Hartley, J. Marrow, P. G. Bruce, *Nat. Mater.* **2019**, 18, 1105.
- [15] J. A. Lewis, F. J. Q. Cortes, Y. Liu, J. C. Miers, A. Verma, B. S. Vishnugopi, J. Tippens, D. Prakash, T. S. Marchese, S. Y. Han, C. Lee, P. P. Shetty, H. W. Lee, P. Shevchenko, F. De Carlo, C. Saldana, P. P. Mukherjee, M. T. McDowell, *Nat. Mater.* **2021**, 20, 503-510.
- [16] a) S. Wang, H. Xu, W. Li, A. Dolocan, A. Manthiram, *J. Am. Chem. Soc.* **2018**, 140, 250; b) Z. Zhang, S. Wenzel, Y. Zhu, J. Sann, L. Shen, J. Yang, X. Yao, Y. Hu, C. Wolverton, H. Li, L. Chen, J. Janek, *ACS Appl. Energy Mater.* **2020**, 3, 7427.
- [17] a) X. Wang, L. Fu, R. Zhan, L. Wang, G. Li, M. Wan, X. Wu, Z. W. Seh, L. Wang, Y. Sun, *ACS Appl. Mater. Interfaces* **2021**, 13, 13354-13361; b) T. Xu, P. Gao, P. Li, K. Xia, N. Han, J. Deng, Y. Li, J. Lu, *Adv. Energy Mater.* **2020**, 10, 1902343.
- [18] S. Lou, F. Zhang, C. Fu, M. Chen, Y. Ma, G. Yin, J. Wang, *Adv. Mater.* **2021**, 33, 2000721.
- [19] a) H. Koshikawa, S. Matsuda, K. Kamiya, M. Miyayama, Y. Kubo, K. Uosaki,

- K. Hashimoto, S. Nakanishi, *J. Power Sources* **2018**, 376, 147; b) T. Krauskopf, H. Hartmann, W. G. Zeier, J. Janek, *ACS Appl. Mater. Interfaces* **2019**, 11, 14463.
- [20] a) X. Liu, R. Garcia-Mendez, A. R. Lupini, Y. Cheng, Z. D. Hood, F. Han, A. Sharafi, J. C. Idrobo, N. J. Dudney, C. Wang, C. Ma, J. Sakamoto, M. Chi, *Nat. Mater.* **2021**, DOI: 10.1038/s41563-021-01019-x; b) C. Wang, H. Jin, Y. Zhao, *Small* **2021**, 17, 2100974.
- [21] J. Meng, F. Chu, J. Hu, C. Li, *Adv. Funct. Mater.* **2019**, 29, 1902220.
- [22] M. Wang, J. B. Wolfenstine, J. Sakamoto, *Electrochim. Acta* **2019**, 296, 842.
- [23] Q. Ma, C. L. Tsai, X. K. Wei, M. Heggen, F. Tietz, J. T. S. Irvine, *J. Mater. Chem. A* **2019**, 7, 7766.
- [24] K. Cao, Q. Ma, F. Tietz, B. B. Xu, M. Yan, Y. Jiang, *Sci. Bull.* **2020**, 66, 179-186.
- [25] W. Li, Z. Yao, Y. Zhong, C. Zhou, X. Wang, X. Xia, D. Xie, J. Wu, C. Gu, J. Tu, *J. Mater. Chem. A* **2019**, 7, 10231.

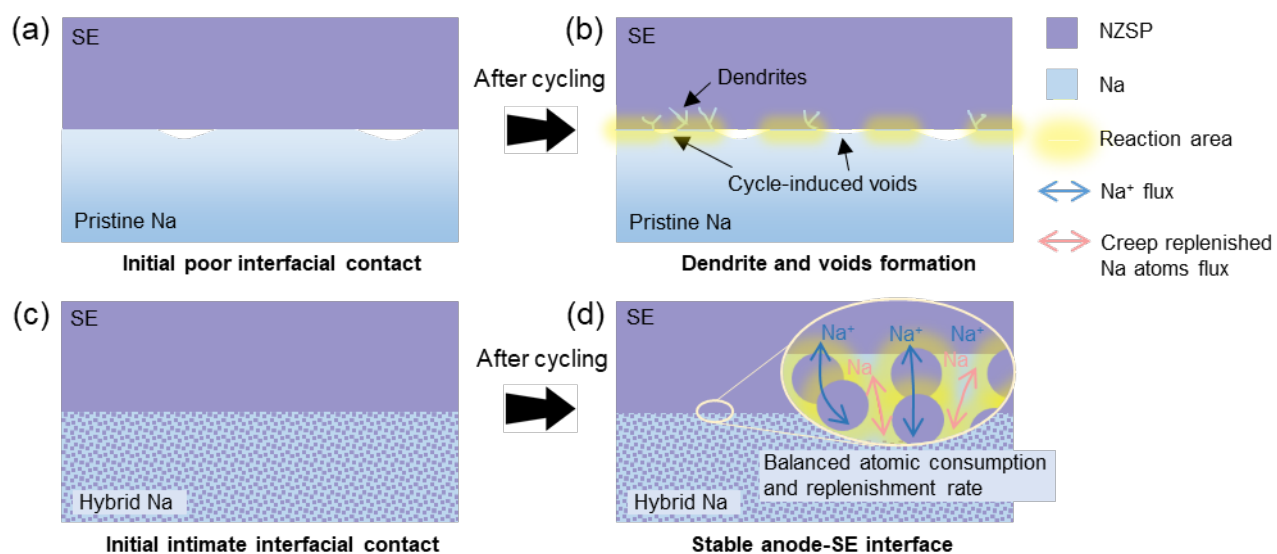


Figure 1. Schematic illustrations of cycle-induced interface evolution in pristine Na/SE interface (a, b) and hybrid Na/SE interface (c, d).

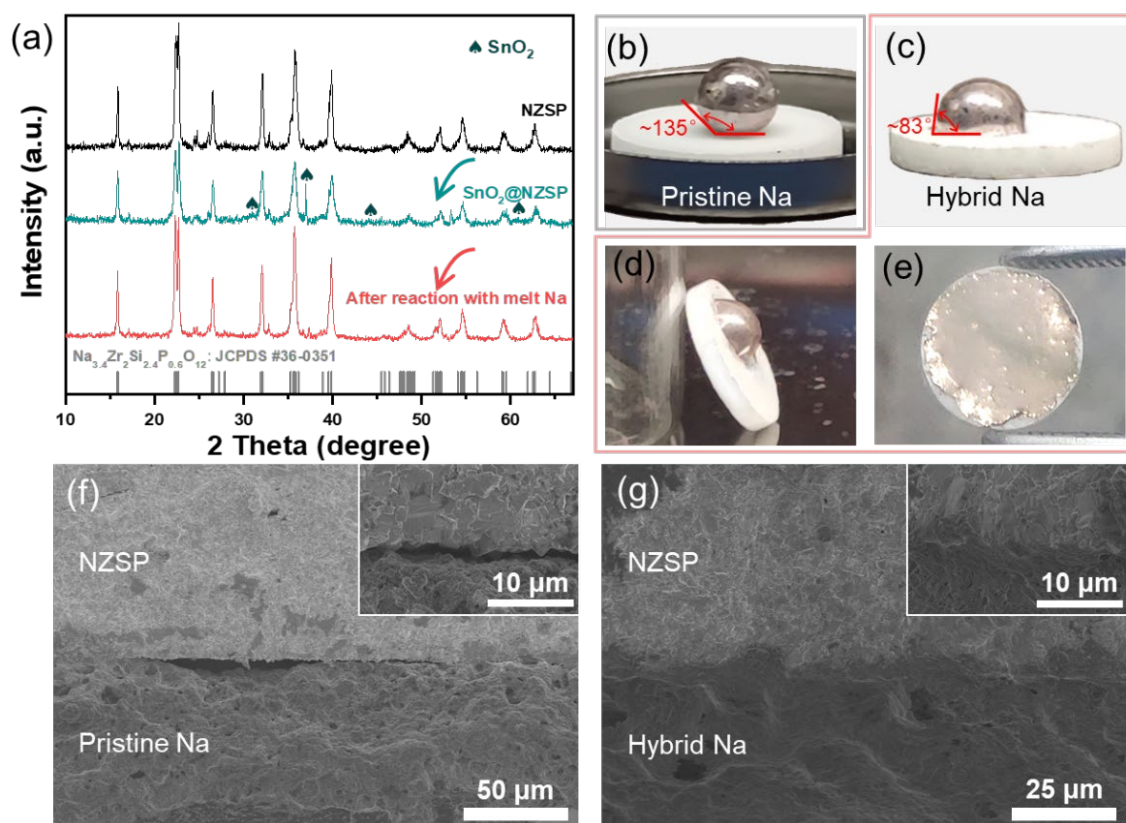


Figure 2. XRD patterns of $\text{SnO}_2@\text{NZSP}$ before and after mixing with molten Na (a). Comparison of the wetting behaviors of molten Na (b) and hybrid Na (c-e) on NZSP pellet. SEM images of the initial pristine Na/SE interface (f) and hybrid Na/SE interface (g).

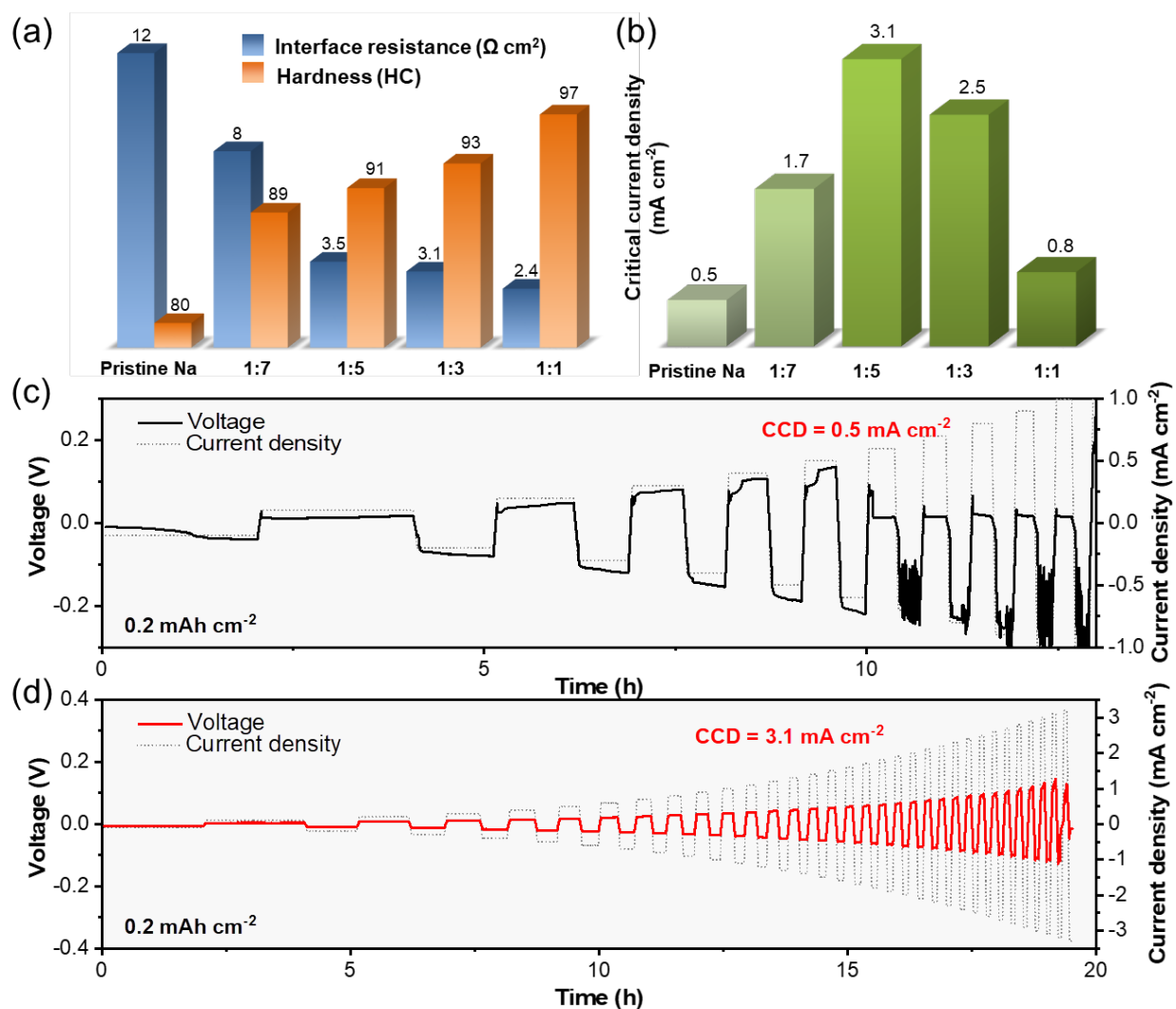


Figure 3. Hardness and interface resistance (a), as well as the CCD (b) of hybrid Na with different NZSP contents and pristine Na. The time-dependent voltage curves of pristine Na (c) and hybrid Na (d) symmetric cells at room temperature under a step-increased current density (the capacity was fixed at 0.2 mAh cm^{-2}).

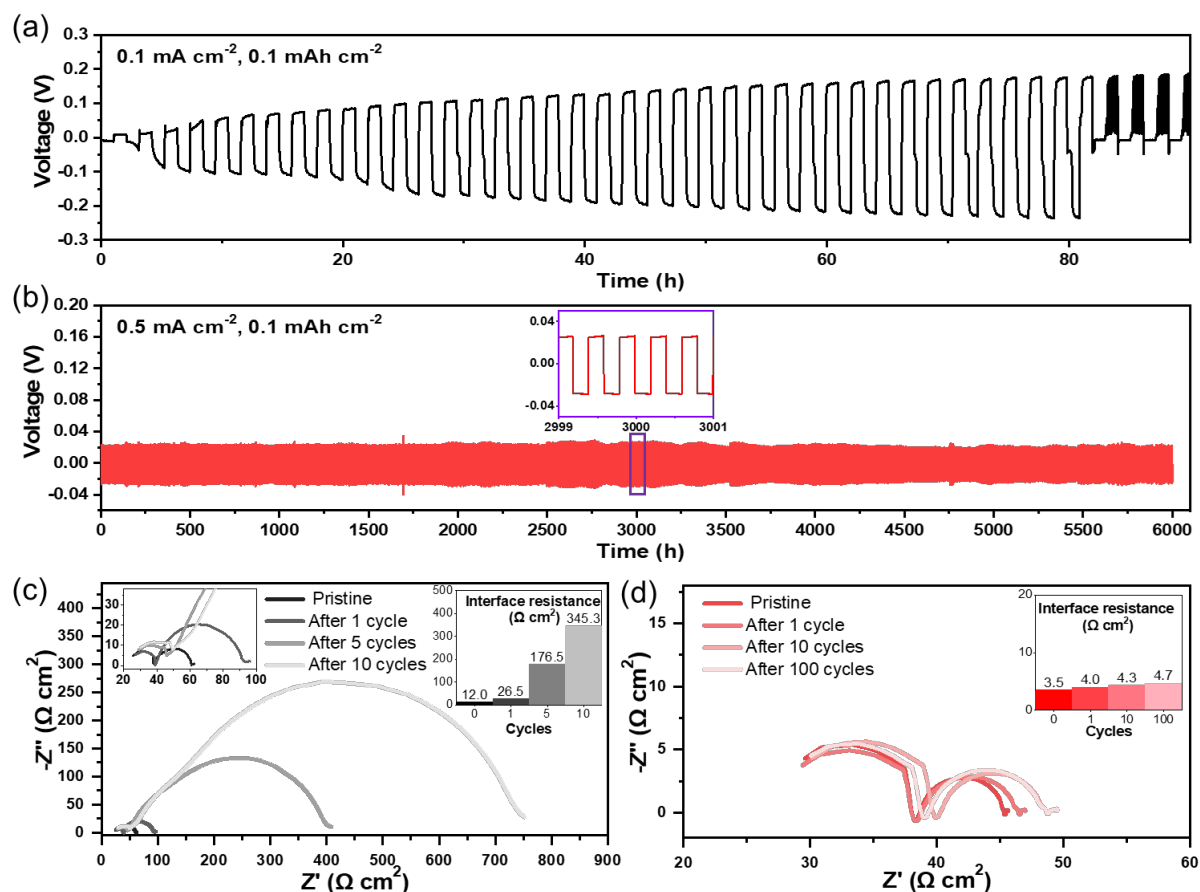


Figure 4. Galvanostatic cycling performance of the Na symmetric cell (a) and h-Na symmetric cell (b) at room temperature. EIS profiles of the symmetric Na cell (c) and h-Na cell (d) during a galvanostatic cycle test. The inset shows the calculated interface resistance.

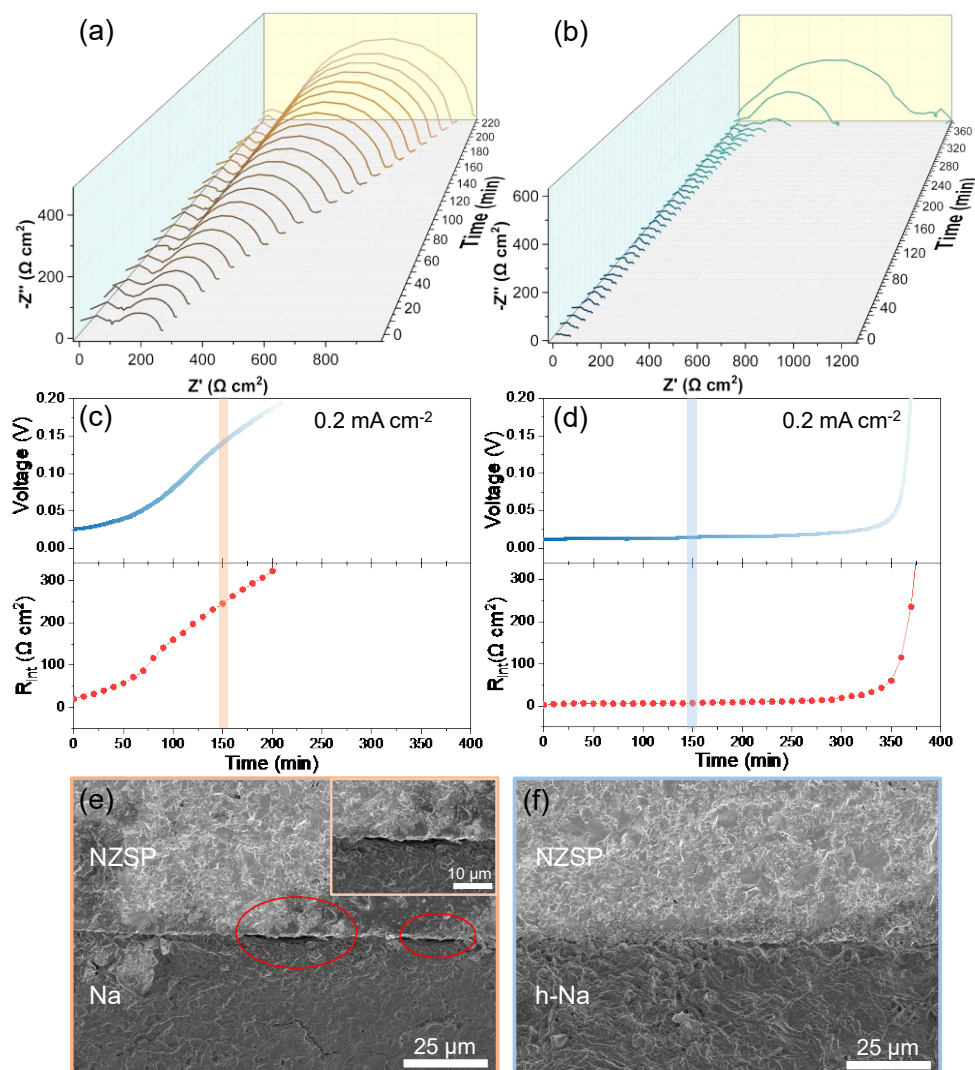


Figure 5. Operando galvanostatic electrochemical impedance spectroscopy (GEIS) of pristine Na (a) and h-Na (b) symmetric cells at 0.2 mA cm^{-2} . Voltage profile and the corresponding fitted interface resistance of the symmetric Na cell (c) and h-Na cell (d). Morphology of pristine Na/SE (e) and h-Na/SE (f) interface after 150 min stripping at 0.2 mA cm^{-2} .

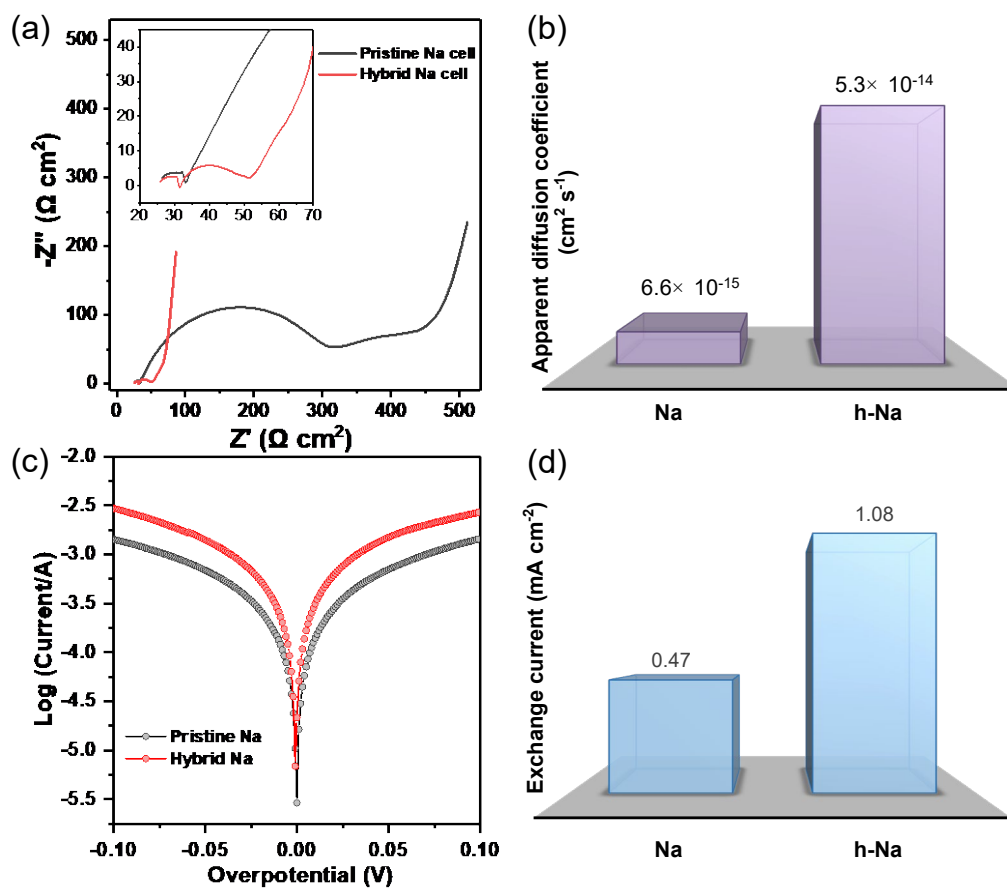


Figure 6. Nyquist plots of the pristine Na cell and h-Na cell (a), and the corresponding calculated Na^+ apparent diffusion coefficient (b). Tafel plots of the symmetric Na cell and h-Na cell (c), and the corresponding calculated exchange current density (d).

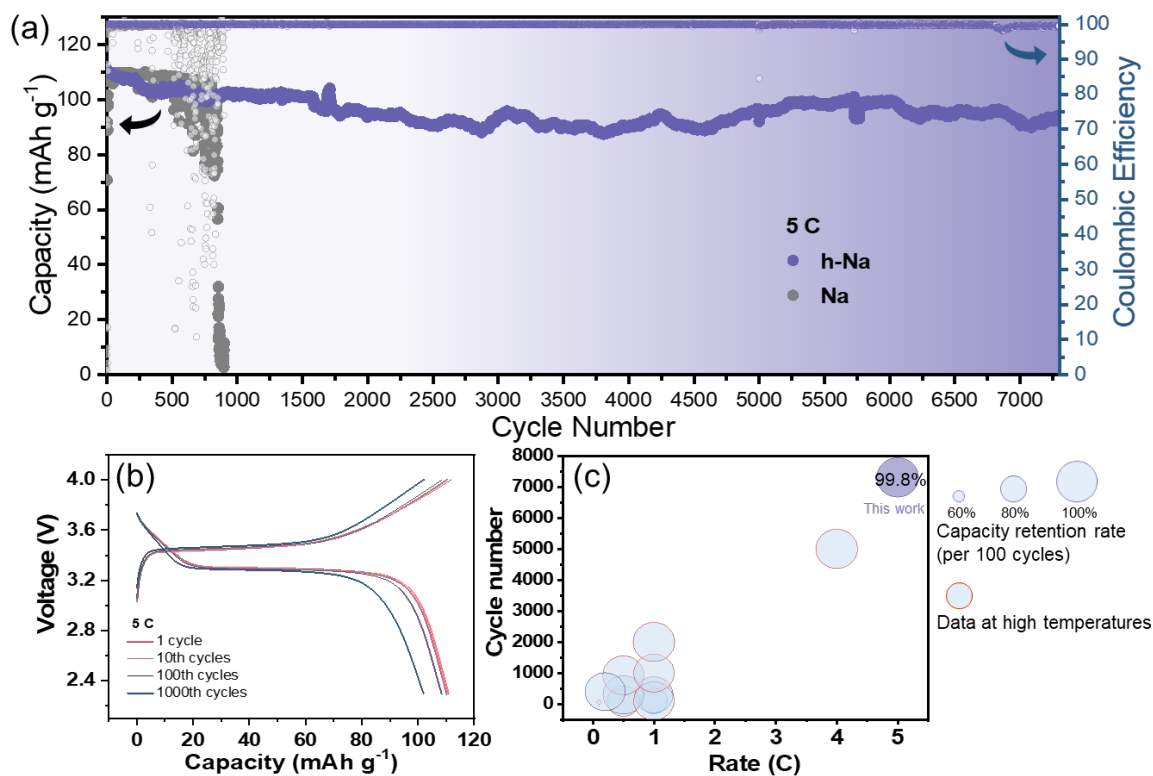


Figure 7. (a) The galvanostatic cycling performance of the NVP/NZSP/Na and NVP/NZSP/h-Na cells under a high current rate of 5 C at room temperature. (b) The charge/discharge curves for the 1st, 10th, 100th and 1000th cycle of the h-Na cell. (c) The performance comparison of this work and recent reported solid-state sodium batteries with NVP cathodes (the size of the circle represents the capacity retention rate per 100 cycles, and the red circle represents the data was not measured at room temperature), the corresponding table is listed in Table S1.

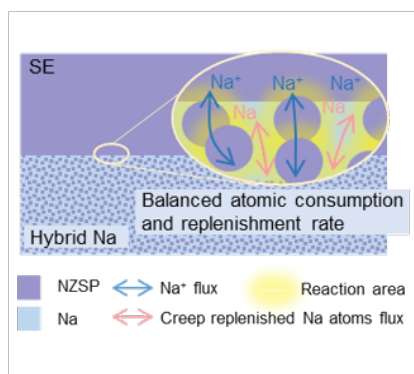
The table of contents:

Hybrid design of bulk-Na metal anode to minimize cycle-induced interface deterioration of solid Na metal battery

*Keshuang Cao, Xitong Zhao, Jian Chen, Ben Bin Xu, Muhammad Wakil Shahzad, Wenping Sun, Hongge Pan, Mi Yan, Yinzhu Jiang**

By incorporating ion-conducting phase into metallic Na matrix, a hybrid bulk Na metal anode is designed to achieve a highly stable Na metal anode-solid electrolyte interface in solid-state batteries. Profiting from the balanced consumption and replenishment rate of Na atoms, cycle-induced interface deterioration is minimized, resulting in ultra-long lifespan in the symmetric cell and full cell.

ToC figure:



Supporting Information

Hybrid design of bulk-Na metal anode to minimize cycle-induced interface deterioration of solid Na metal battery

*Keshuang Cao, Xitong Zhao, Jian Chen, Ben Bin Xu, Muhammad Wakil Shahzad, Wenping Sun, Hongge Pan, Mi Yan, Yinzhu Jiang**

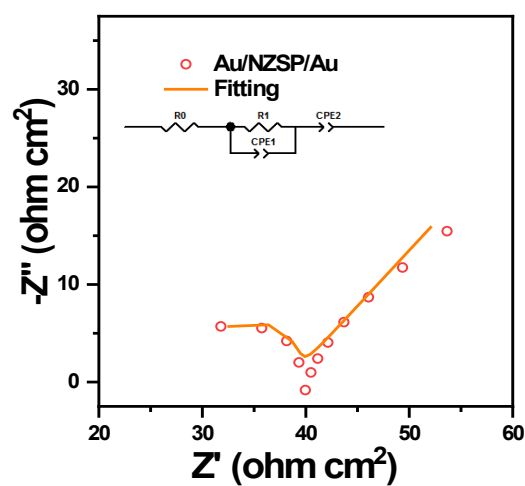


Figure S1. Nyquist plot of sintered NZSP pellet with gold blocking electrodes. The diameter of NZSP pellet is 1.114 cm, and the thickness is 0.162 cm. In the equivalent circuit, the sum of the bulk resistance (R_0) and the grain-boundary resistance (R_1) represents the total resistance (R_{total}) of the sample. The σ_{total} of NZSP is calculated as $4.1 \times 10^{-3} \text{ S cm}^{-1}$ at 25 °C.

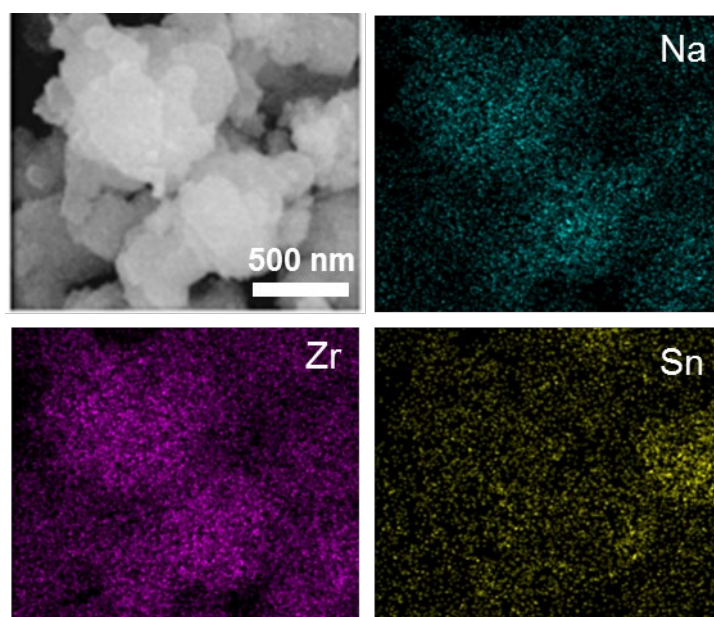


Figure S2. SEM image and EDS mapping of $\text{SnO}_2@\text{NZSP}$.

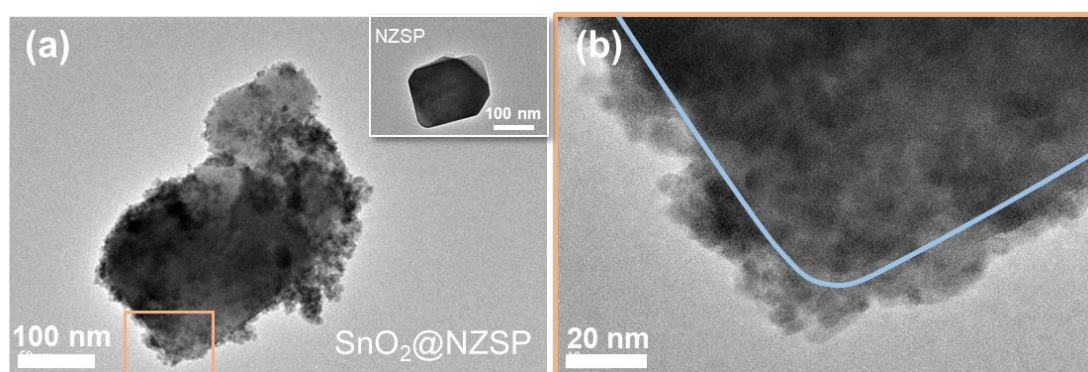


Figure S3. (a) Low-magnification and (b) high-magnification TEM images of $\text{SnO}_2@\text{NZSP}$. The inset in the upper right corner of Figure S3a is the TEM image of pristine NZSP particle.

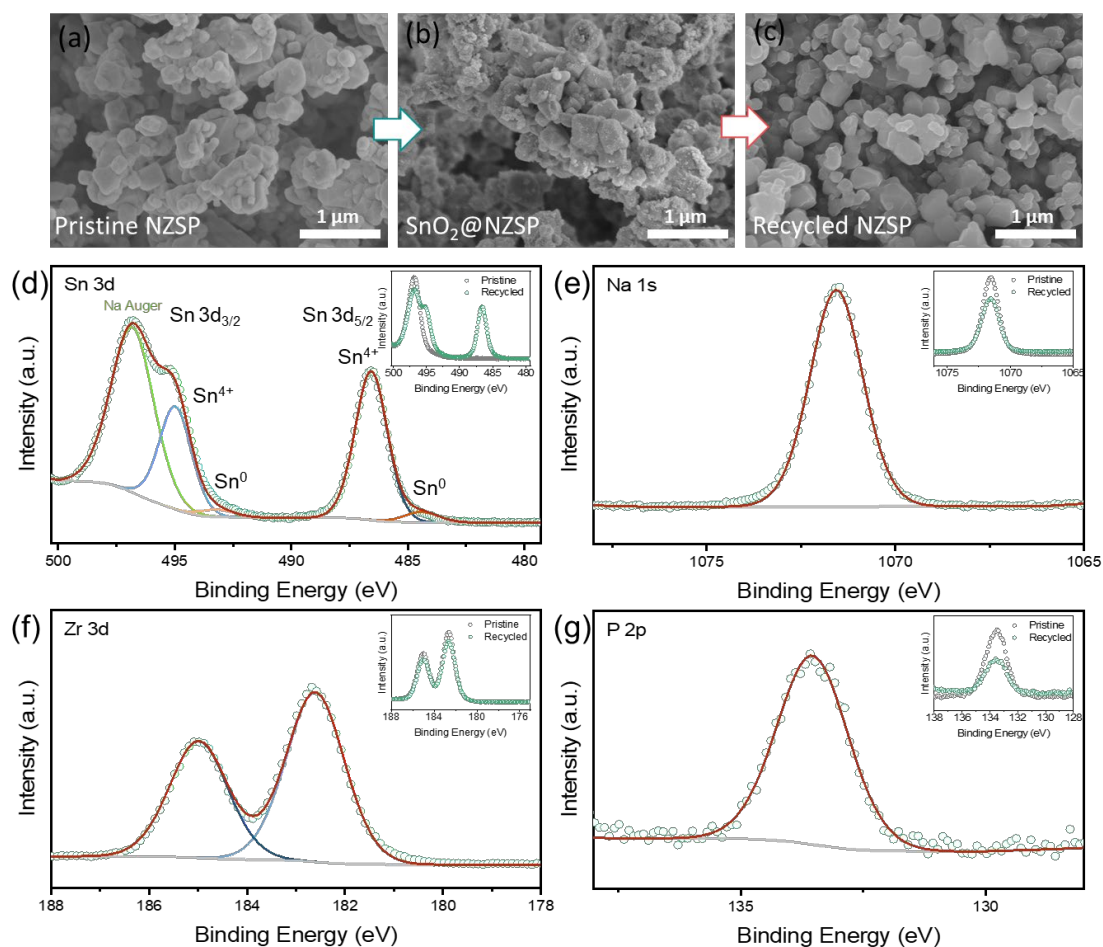


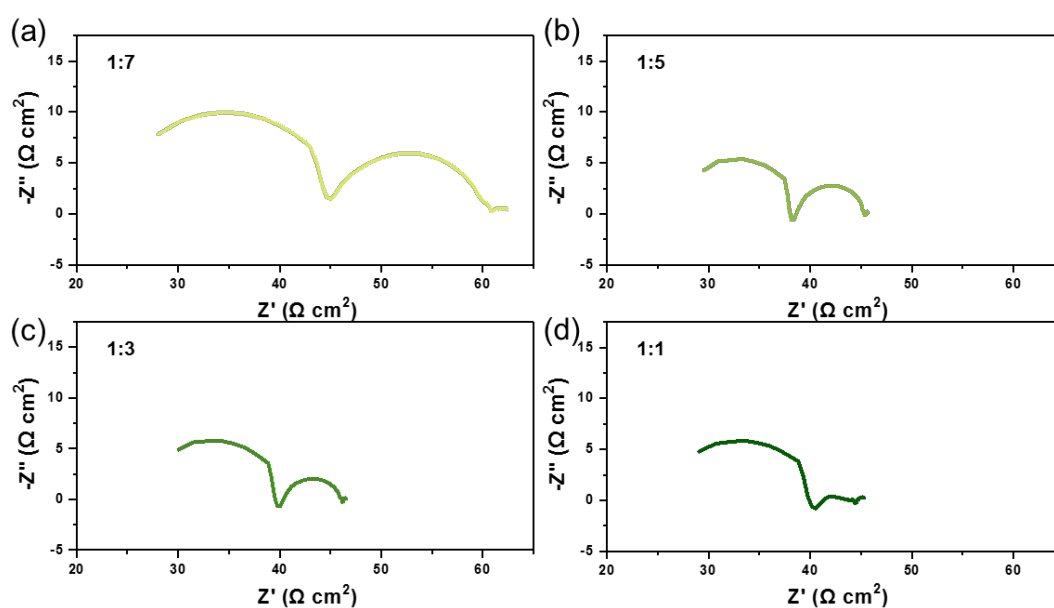
Figure S4. SEM images of pristine NZSP (a), $\text{SnO}_2@\text{NZSP}$ (b) and recycled NZSP (c). Recycled NZSP is the NZSP powder obtained after washing the NZSP/Na mixture with alcohol. XPS spectra of (d) Sn 3d, (e) Na 1s, (f) Zr 3d and (g) P 2p of the recycled NZSP surface. The inset in the upper right corner of the figure is a comparison between pristine NZSP and recycled NZSP. The high-resolution XPS spectra of Sn 3d consisting of two peaks located at 495.0 and 486.6 eV, which can be assigned to Sn^{4+} , and two another peaks at 493.1, 484.4 eV attributed to metallic Sn.^[1] The peak at 496.8 eV is assigned to Auger peak of Na. Sn^{4+} may come from the residual SnO_2 on the surface of $\text{SnO}_2@\text{NZSP}$, and metallic Sn may come from the residual Na-Sn alloy. Na 1s, P 2p and Zr 3d peaks show no change in shape and symmetry after mixed with Na metal (Figure R1b, c, d).



Figure S5. Molten sodium cannot wet on the NZSP pellet, and rolls off from the NZSP pellet when the pellet is slightly tilted. The NZSP pellet and rolled Molten Na are shown in this photograph.



Figure S6. Hybrid Na with different NZSP content spread on NZSP pellet.



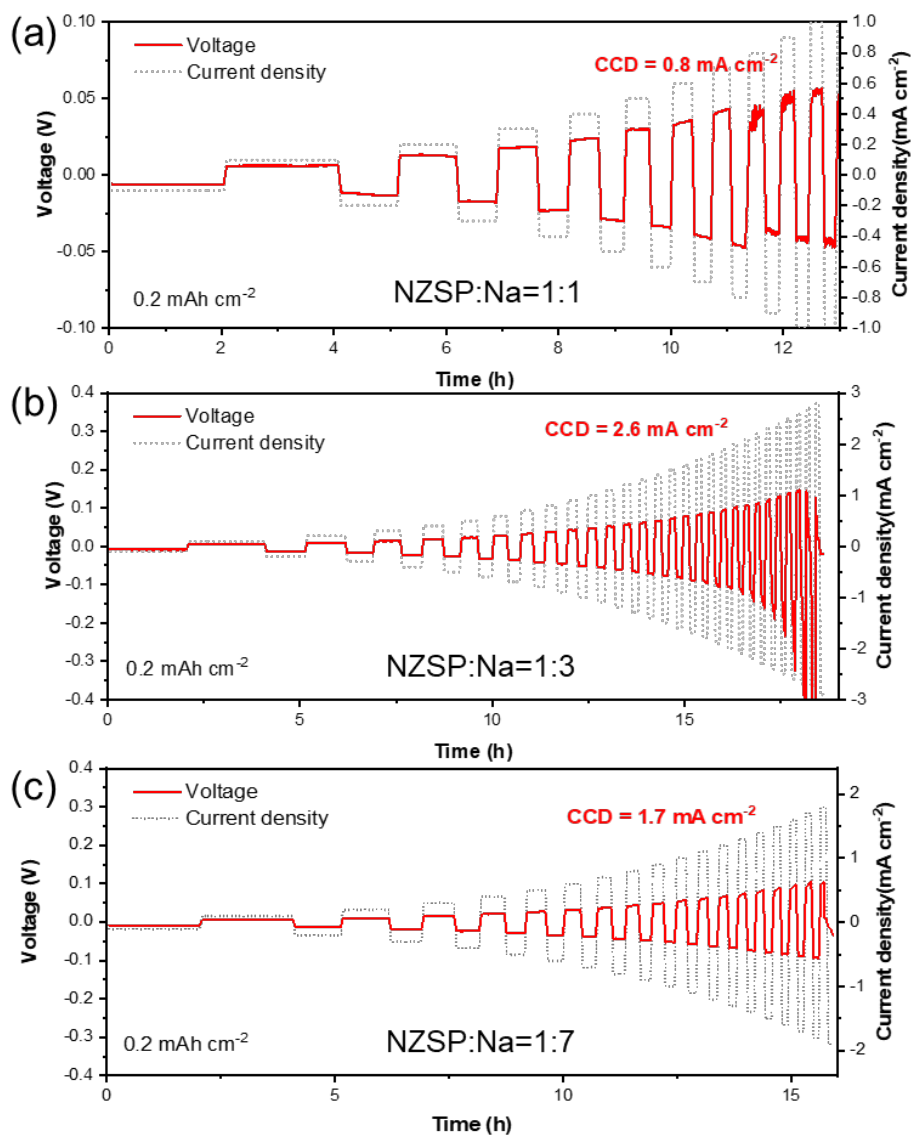


Figure S8. CCD tests of hybrid Na with other contents.

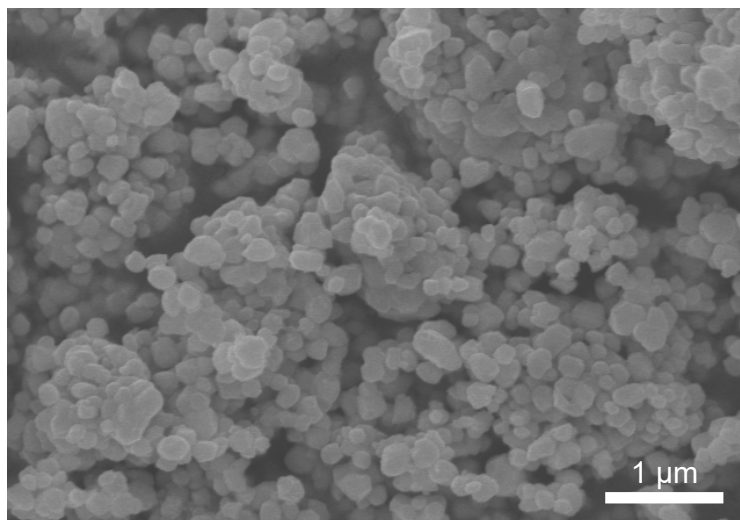


Figure S9. SEM image of ZrO₂ powder.



Figure S10. $\text{ZrO}_2\text{-Na}$ spread on NZSP pellet.

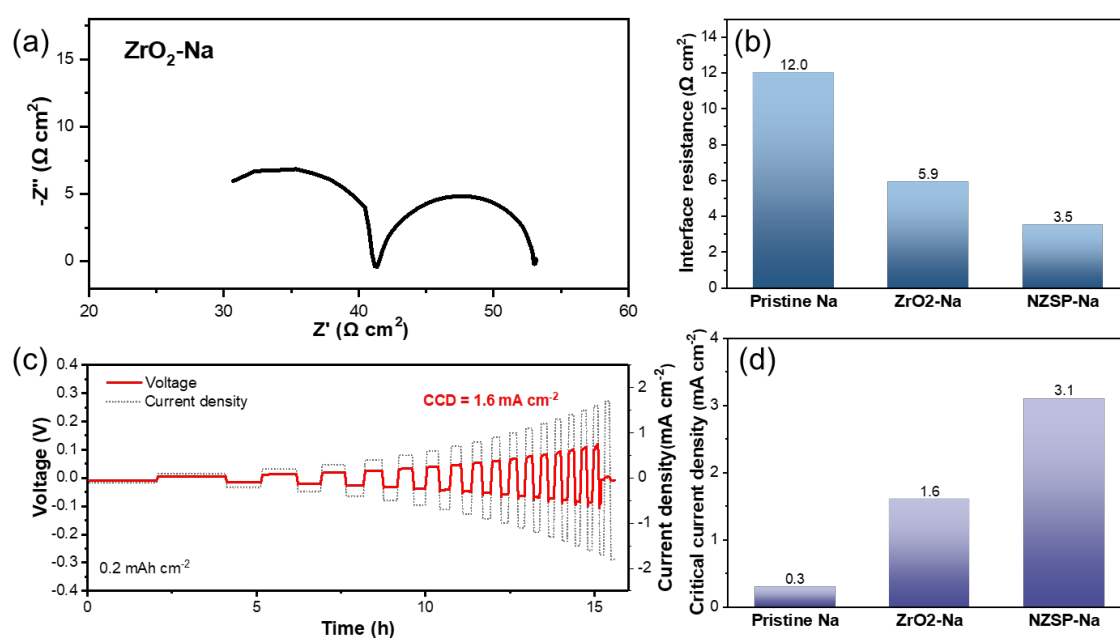


Figure S11. Impedance spectrum (a) and CCD test (c) of $\text{ZrO}_2\text{-Na}$, and comparison with pristine Na and NZSP-Na (b, d).

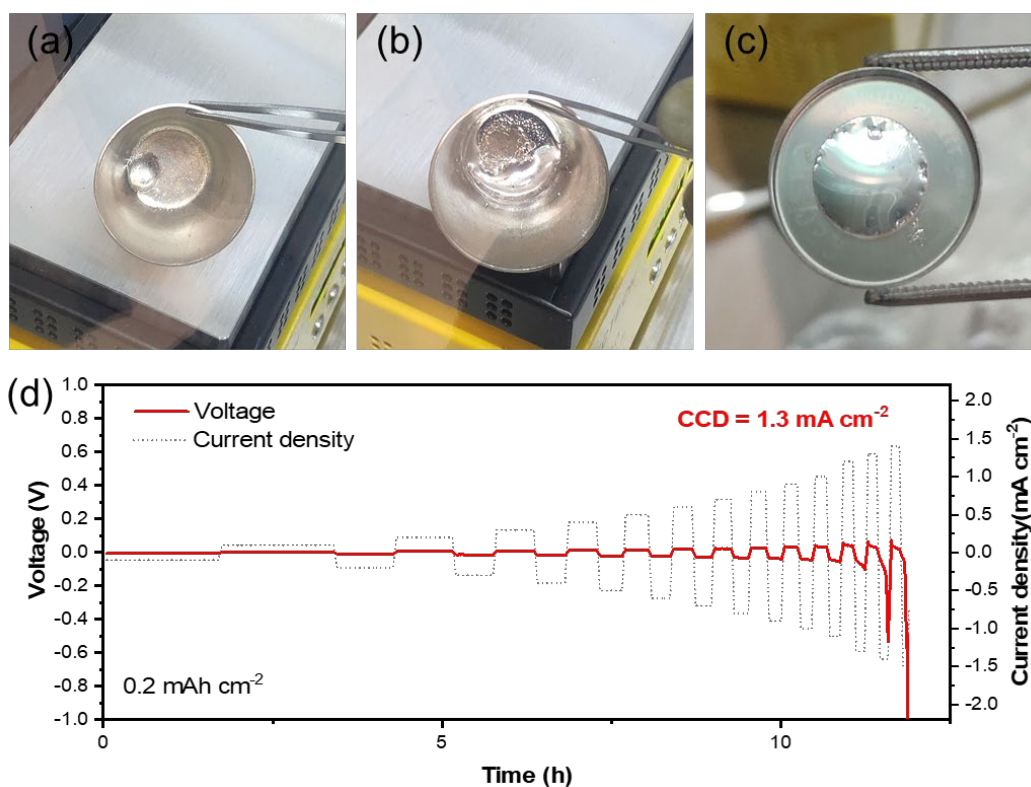


Figure S12. (a) SnO_2 and molten Na in the initial state. (b) The mixture after stirring. (c) $\text{SnO}_2\text{-Na}$ spread on NZSP pellet. (d) The CCD test result of the $\text{SnO}_2\text{-Na}$ symmetric cell. The mass fraction of the SnO_2 coating layer in $\text{SnO}_2\text{@NZSP}$ is measured to be 8.62 wt% by the ICP-OES measurement. So 0.0069 g SnO_2 is mixed with 0.4 g Na to be consistent with the content of SnO_2 in h-Na. The CCD of the $\text{SnO}_2\text{-Na}$ symmetric cell is 1.3 mA cm^{-2} .

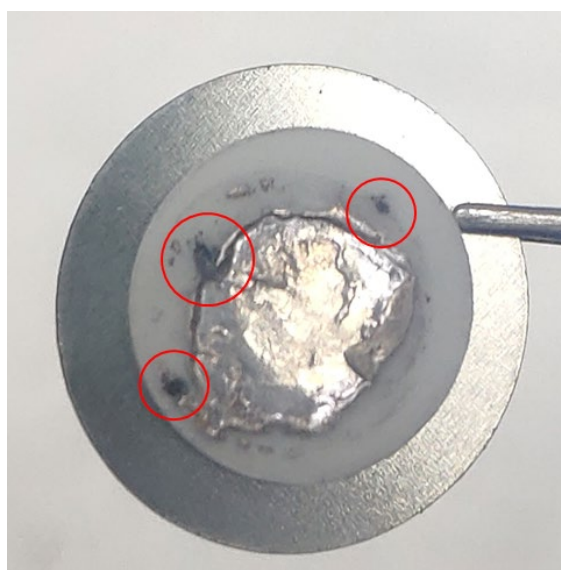


Figure S13. Optical photo of NZSP in failed pristine Na symmetric cell.

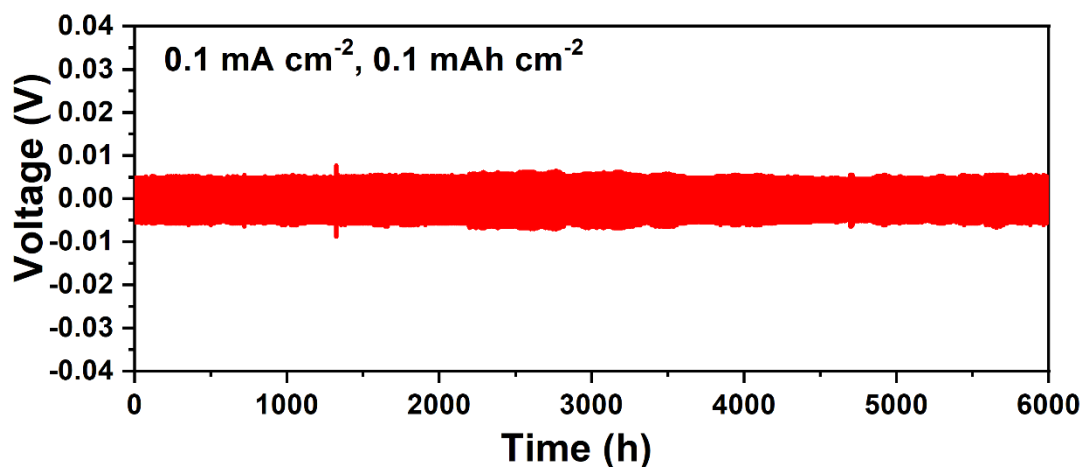


Figure S14. Long-term cycling measurements of symmetric hybrid Na cell in 0.1 mA cm⁻², 0.1 mAh cm⁻².

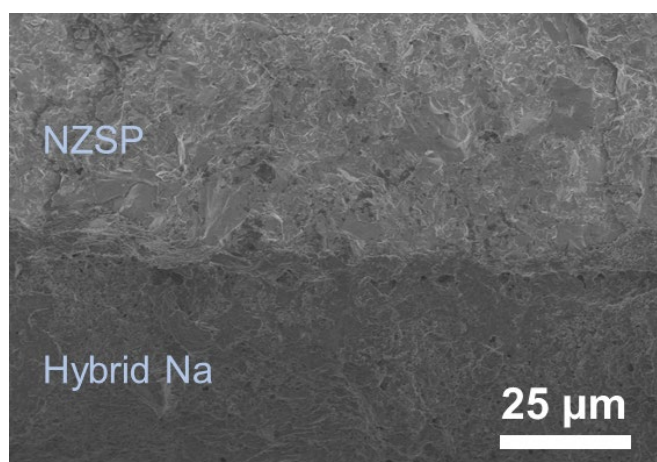


Figure S15. Hybrid Na/SE interface after 100 cycles.

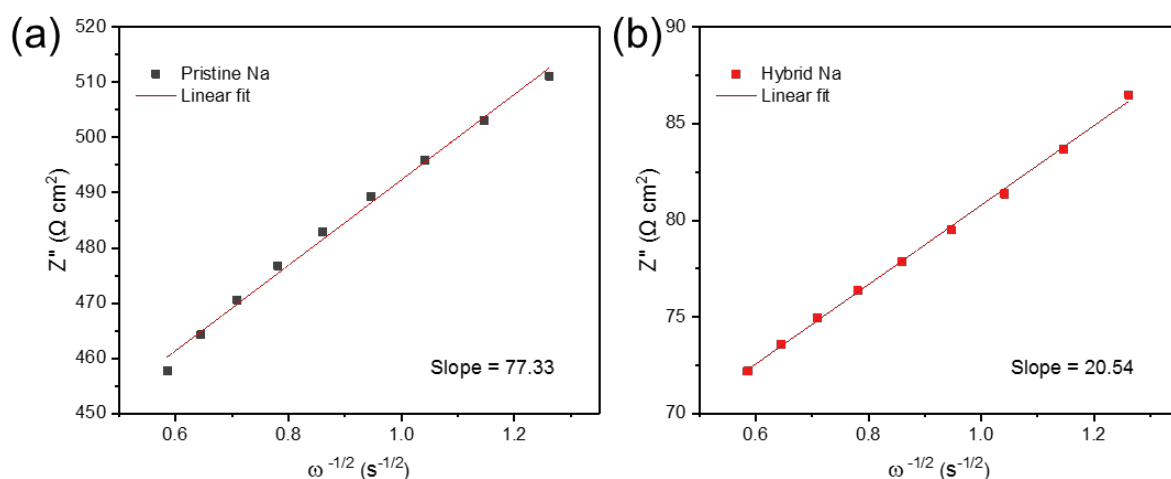


Figure S16. Fitting the low-frequency region of the impedance spectrum in Figure 6a, the Warburg coefficient can be calculated from the slope, and then the Na⁺ apparent diffusion coefficient can be obtained.

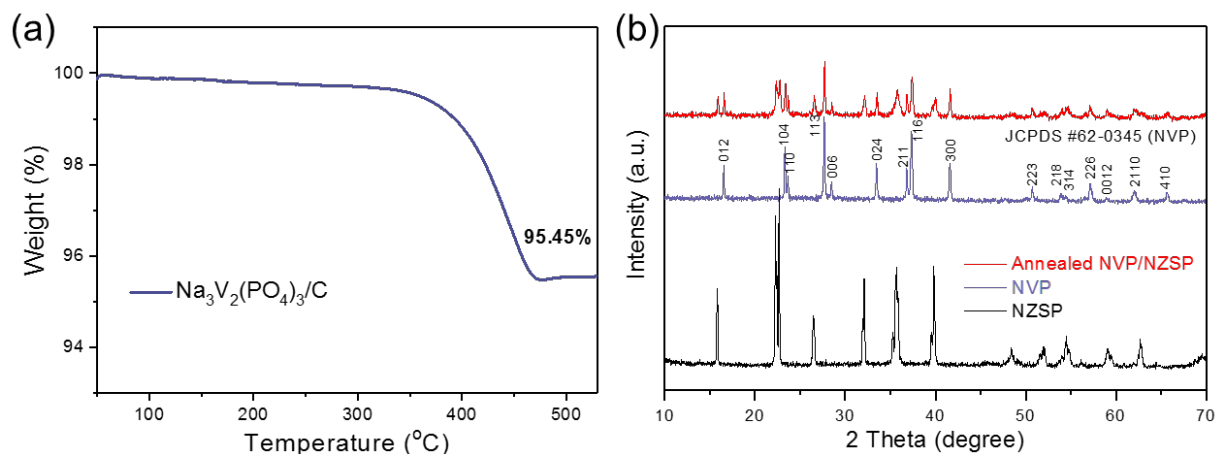


Figure S17. (a) The thermogravimetric curve of NVP. (b) XRD patterns of NVP, NZSP and annealed NVP/NZSP.

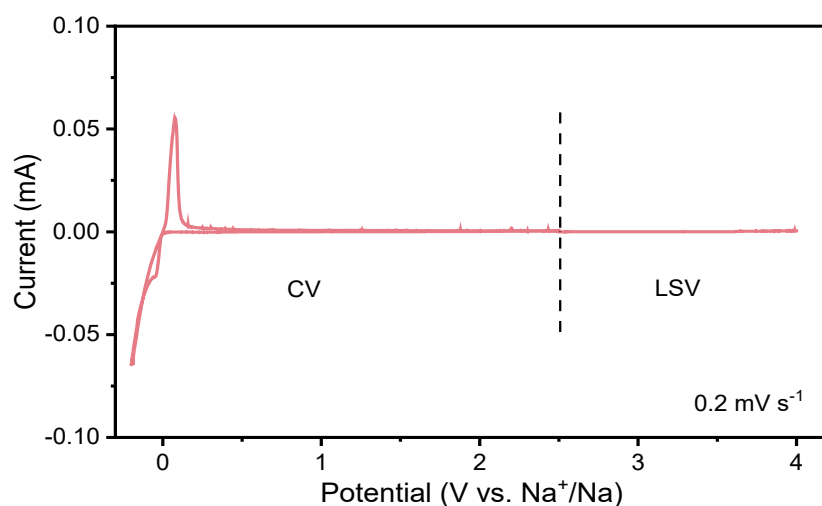


Figure S18. Cyclic voltammetry (CV) and linear sweep voltammetry (LSV) of the Au/NZSP/Na cell at room temperature. A couple of oxidation and reduction peaks near 0 V correspond to the Na plating and stripping, and NZSP can also maintain electrochemical stability at 4V (vs. Na^+/Na), indicating that NZSP is electrochemically stable in the NVP/NZSP/Na cell test.

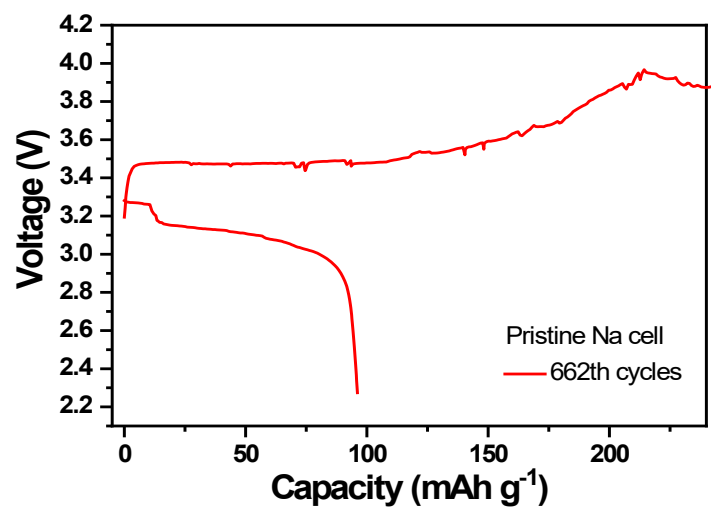


Figure S19. The charge and discharge curve of pristine Na cell at 662th cycles.

Table S1. Comparison of electrochemical performances between this work and recently reported solid-state sodium batteries based on NVP cathodes.

Strategy	Solid-state electrolytes	Rate	Working temperature	Cycle number	Capacity retention rate (per 100 cycles)	Ref.
Coating TiO ₂ on SE	Na ₃ Zr ₂ Si ₂ PO ₁₂	0.1 C	60 °C	60	50.9%	[2]
Coating AlF ₃ on SE	Na ₃ Zr ₂ Si ₂ PO ₁₂	1 C	25 °C	100	80.7%	[3]
Composite Na/carbon cloth metal anode	PEO ₂₀ NaFSI	4 C	80 °C	5000	99.6%	[4]
Graphene-like interlayer on SE	Na ₃ Zr ₂ Si ₂ PO ₁₂	1 C	25 °C	300	95.1%	[5]
Flexible solid electrolyte with a multilayer structure	NZSP/PVDF-HFP	0.5 C	60 °C	100	87.5%	[6]
GPEs membrane with Ti ₃ C ₂ T _x MXene filler	Gel polymer electrolytes	0.5 C	25 °C	300	98.4%	[7]
In situ polymerization process	PEGDMA-NaFSI-SPE	0.5 C	60 °C	925	99.1%	[8]
Plastic-crystal electrolyte interphase	Na ₃ Zr ₂ Si ₂ PO ₁₂	1 C	50 °C	100	98%	[9]
Coating β/β''-Al ₂ O ₃ membrane with PVdF-HFP-based GPE	Hybrid inorganic ionic conductor/GPE composite	1 C	60 °C	1000	97.9%	[10]
Remove residual solvent in SPE	PEO/NaFSI-Al ₂ O ₃ -AQ electrolytes	1 C	80 °C	2000	99.65%	[11]
In-situ thermal cured technique	PPEGMA-based gel polymer electrolyte	0.2 C	25 °C	400	97.8%	[12]
Hybrid Na metal anode	Na _{3.4} Zr ₂ Si _{2.4} P _{0.6} O ₁₂	5 C	25 °C	7300	99.8%	This work

References

- [1] J. Ni, X. Zhu, Y. Yuan, Z. Wang, Y. Li, L. Ma, A. Dai, M. Li, T. Wu, R. Shahbazian-Yassar, J. Lu, L. Li, *Nat. Commun.* **2020**, 11, 1212.
- [2] J. Yang, Z. Gao, T. Ferber, H. Zhang, C. Guhl, L. Yang, Y. Li, Z. Deng, P. Liu, C. Cheng, R. Che, W. Jaegermann, René Hausbrand, Y. Huang, *J. Mater. Chem. A* **2020**, 8, 7828.
- [3] X. Miao, H. Di, X. Ge, D. Zhao, P. Wang, R. Wang, C. Wang, L. Yin, *Energy Storage Mater.* **2020**, 30, 170.
- [4] C. Zao, L. Liu, Y. Lu, M. Wagemaker, L. Chen, Y.-S. Hu, *Angew. Chem. Int. Ed.* **2019**, 58, 17026.
- [5] E. Matios, H. Wang, C. Wang, X. Hu, X. Lu, J. Luo, W. Li, *ACS Appl Mater Interfaces* **2019**, 11, 5064.
- [6] W. Ling, N. Fu, J. Yue, X. Zeng, Q. Ma, Q. Deng, Y. Xiao, L. Wan, Y. Guo, X. Wu, *Adv. Energy Mater.* **2020**, 10, 1903966.
- [7] X. Wang, X. Wang, J. Chen, Y. Zhao, Z. Mao, D. Wang, *Solid State Ionics* **2021**, 365, 115655.
- [8] Y. Yao, Z. Wei, H. Wang, H. Huang, Y. Jiang, X. Wu, X. Yao, Z. Wu, Y. Yu, *Adv. Energy Mater.* **2020**, 10, 1903698.
- [9] H. Gao, L. Xue, S. Xin, K. Park, J. B. Goodenough, *Angew. Chem. Int. Ed.* **2017**, 56, 5541.
- [10] D. Lei, Y. He, H. Huang, Y. Yuan, G. Zhong, Q. Zhao, X. Hao, D. Zhang, C. Lai, S. Zhang, J. Ma, Y. Wei, Q. Yu, W. Lv, Y. Yu, B. Li, Q. Yang, Y. Yang, J. Lu, F. Kang,

Nat. Commun. **2019**, 10, 4244.

[11] L. Liu, X. Qi, S. Yin, Q. Zhang, X. Liu, L. Suo, H. Li, L. Chen, Y. Hu, *ACS Energy Lett.* **2019**, 4, 1650.

[12] G. Chen, K. Zhang, Y. Liu, L. Ye, Y. Gao, W. Lin, H. Xu, X. Wang, Y. Bai, C. Wu, *Chem. Eng. J.* **2020**, 401, 126065.